Enhanced Material Assimilation in a Toroidal Plasma Using Mixed $H_2 + Ne$ Pellet Injection and Implications to ITER

A. Matsuyama*
National Institutes for Quantum Science and Technology, Rokkasho, Aomori 039-3212, Japan

R. Sakamoto, R. Yasuhara, H. Funaba, H. Uehara, I. Yamada, T. Kawate, and M. Goto
National Institute for Fusion Science, Toki, Gifu 509-5292, Japan

(Received 15 July 2022; revised 19 September 2022; accepted 19 October 2022; published 14 December 2022)

The ablation and assimilation of cryogenic pure H_2 and mixed $H_2 + Ne$ pellets, which are foreseen to be used by the ITER tokamak for mitigating thermal and electromagnetic loads of major disruptions, are observed by spatially and temporally resolved measurements. It is experimentally demonstrated that a small fraction (here ≈5%) of neon added to hydrogenic pellets enhances the core density assimilation with reduced outward transport for the low magnetic-field side injection. This is consistent with theoretical expectations that line radiation increased by doped neon in dense plasmoids suppresses the plasmoid pressure and reduces the $\vec{E} \times \vec{B}$ transport of the ablated material.

DOI: 10.1103/PhysRevLett.129.255001

Introduction.—Plasma-material interaction is an important subject in various fields of plasma physics. Solid materials immersed in a hot magnetized plasma are ablated, which can cause intense perturbations that often lead to large-scale dynamics. In the field of magnetically confined fusion plasmas, solid pellets are injected for controlling the electron density [1] and for delivering desired materials into a plasma [2–5]. In the ITER tokamak, a massive material injection scheme, called shattered pellet injection (SPI) [6], is currently being designed, which is aimed at rapidly dissipating the plasma energy for protecting material walls when the discharge is terminated by unintended plasma instabilities [7–9]. Reliable and successful "disruption mitigation" has been recognized as a major challenge from the early experimental campaigns planned at ITER [10].

In this Letter, we explore the physics relevant to cryogenic pure H_2 and mixed $H_2 + Ne$ pellets as foreseen to be used by the ITER SPI. These materials are selected for dilution cooling of the plasma by massive hydrogen injection [11] to raise the electron density to avoid hot-tail runaway electron generation [12], and for radiative cooling to dissipate the thermal and magnetic energies of a burning plasma pulse using line radiation enhanced by neon [13]. While the best mix of these two cooling schemes is under investigation in current tokamaks [13–15], a major difficulty expected in reactor-grade devices such as ITER is that it is not easy to obtain the desired increase in the core density using practical pellet sizes and injection velocities. Especially when pure hydrogenic pellets are injected from the low magnetic-field side (LMFS) of a toroidal plasma, it has been observed that high density plasmoids generated by ablation exhibit radially outward transport [16]. Simply speaking, the basic mechanism is that the magnetic field gradient causes overpressured plasmoids to become polarized, which leads to an $\vec{E} \times \vec{B}$ drift across the magnetic field in the direction down the magnetic field's gradients [17]. The resultant particle losses govern the efficiency of solid fuel injection [18–24], and their impact on the disruption mitigation has also been recently observed in DIII-D for pure deuterium injection [25]. The $\vec{E} \times \vec{B}$ drift is a universal mechanism that governs the cross-field motion of ionizing clouds in laboratory and space applications [26–35]. The experiments described in this Letter were dedicated to comparing the material deposition subject to such transport mechanisms between pure H_2 and mixed $H_2 + Ne$ pellets in magnetically confined laboratory plasmas. This was accomplished by new measurements that are well-resolved in both space and time. Previous numerical work [36] has predicted that the $E \times B$ drift losses are suppressed when a small amount of neon is added to hydrogenic pellets. Here, this prediction is confirmed experimentally for the first time. We demonstrate that the material's outward transport for the LMFS injection is significantly reduced and the core assimilation is enhanced.

Experimental setup.—The experiments were conducted in hydrogen plasmas produced at the Large Helical Device (LHD) heliotron [37] with a major radius of $R = 3.6$ m, an averaged minor radius of $a = 0.6$ m, and a magnetic field strength of 2.75 T. The LHD creates its confining magnetic field solely by three-dimensionally shaped external helical coils. Previous studies [38,39] have shown that LMFS injection of pure H_2 pellets in LHD exhibits outward particle transport and losses, similarly to what limits the fueling efficiency of hydrogenic pellet injection in tokamaks. In this study, we investigate how this behavior is changed by adding a certain amount of neon.

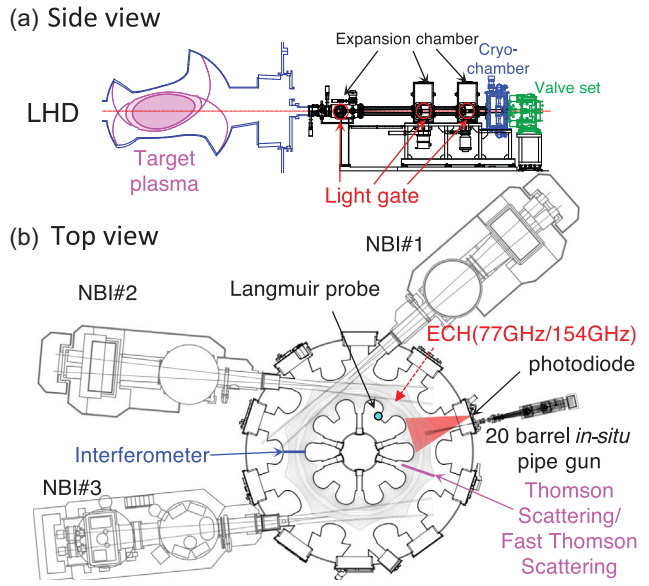

FIG. 1. (a) Schematic of the pellet injector in the Large Helical Device (LHD); (b) top view showing the layout of heating and diagnostic systems.

Cryogenic pellets are injected from the LMFS into a horizontally elongated cross section of the plasma as shown in Fig. 1(a). The 20-barrel *in situ* pipe gun [40] injects cylindrical pellets of 3 mm diameter and length. Helium gas at 5 MPa is used as a propellant, and the pellet speed is observed to decrease from the nominal speed of 1100 m/s for pure H_2 pellets to 886–958 m/s for $H_2:Ne = 20:1$ and 811–886 m/s for $H_2:Ne = 10:1$ mixing ratios. The trend in the measured velocities is consistent with ideal gun theory [41] for a given neon fraction in the fueled gas, implying that there is no significant experimental uncertainty in the amount of injected neon.

As shown in Fig. 1(b), the ablation region is observed by a photodiode with a Balmer α filter (656.28 nm; FWHM = 10 nm). A far infrared interferometer is used to measure line-integrated densities. A Langmuir probe on the divertor plate measures particle fluxes expelled from the core plasma after the pellet injection [42]. The main observations reported in this Letter were made with Thomson scattering (TS) located toroidally 36° downstream from the ablation region. The main TS system [43] with a laser pulse repetition rate of about 30 ms and a spatial resolution of a few cm along the midplane is applied to measure the quasistationary electron density (n_e) and temperature (T_e) profiles after the pellet injection. In addition, we employ fast Thomson scattering (FTS) [44,45], installed at the same port as the main TS system. This novel technique constitutes a unique diagnostic for pellet fueling on the *intermediate* timescale in the sub-ms range—between material ablation and final equilibration. The evolution of the radial profiles of n_e and T_e is imaged during an entire pellet assimilation event by recording about 100 time slices at intervals of 50 μs.

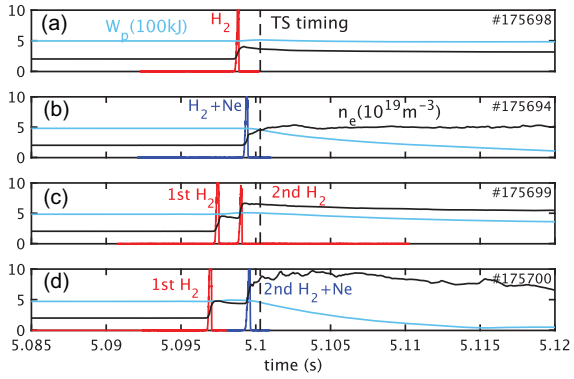

FIG. 2. Single and double pellet injection into ECH discharges. The time evolution of the stored energy W_p and the line-averaged n_e are plotted as cyan and black curves. The red and blue curves are the ablation light emission measured by a photodiode for pure H_2 and mixed $H_2 + Ne$ ($H_2:Ne = 20:1$) pellets, respectively.

Observation.—Figure 2 shows the time traces of pellet injection events in four different discharges maintained by electron cyclotron heating (ECH): (a) a single pure H_2 pellet, (b) a single neon-doped pellet, (c) two H_2 pellets, and (d) a H_2 pellet followed by a neon-doped one. The neon-doped pellets in (b), (d) have the same composition, $H_2:Ne = 20:1$, and the pellet pairs in (c), (d) were injected with a time delay of about 1–2 ms. Figure 3 compares the postinjection profiles measured by the main TS. The timing of the main laser pulses (the dashed lines in Fig. 2) was delayed by 1–2 ms after the ablation light disappeared. The plasma profiles are seen to be equilibrated over the

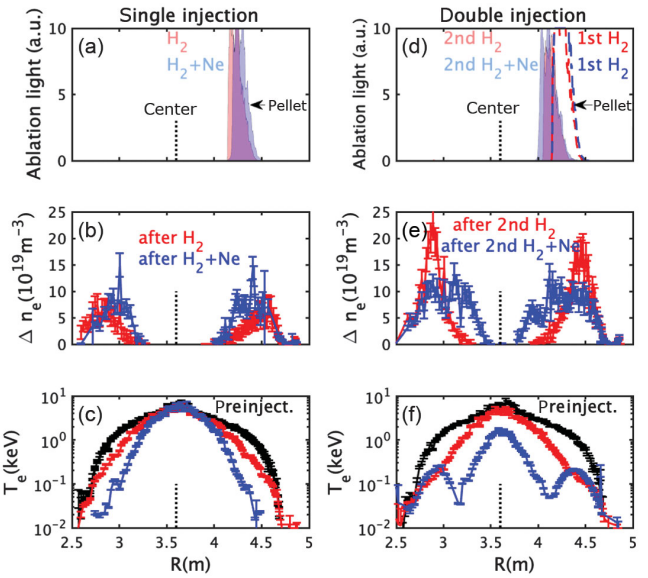

FIG. 3. (a) and (d) Mapping of ablation light along the major radius R. For the sequential injection, the ablation light from the first pellet is shown by the dashed curves. (b) and (e) n_e increment profiles observed after the pellet injection. (c) and (f) Pre- and postinjection T_e profiles.

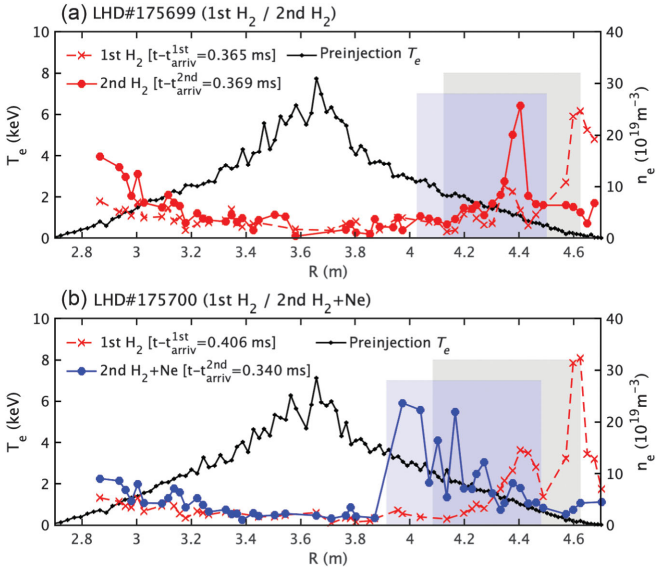

FIG. 4. Radial profiles of the preinjection T_e observed by the main TS (black, left axis) and transient n_e (colors, right axis) observed by fast Thomson scattering (FTS) during the sequential injection of (a) two pure H_2 pellets, and (b) a pure H_2 pellet followed and a mixed $H_2 + Ne$ pellet. The ablation light emission zones that indicate the radial pellet penetration (obtained from the pellet time of flight assuming $\pm 1\%$ errors in the measured velocities) are overlaid in the same plot as gray- and blue-shaded areas for the first and second pellet, respectively. The relative time after the onset of ablation light emissions from the first or second pellets (t_{arriv}) is 0.3–0.4 ms as specified in the legends.

magnetic surfaces as they are symmetric with respect to the plasma center. In spite of the similar ablation light profiles in Fig. 3(a), panels (b) and (c) show that the neon-doped pellet (blue) produces a density rise and causes cooling at a deeper location than pure H_2 pellets (red). This trend is enhanced in the double-injection cases, as one can see in Figs. 3(d)–3(f). While the first pellet (H_2) moderately cools the peripheral region and facilitates a deeper penetration of the second pellet for both cases, using the $H_2 + Ne$ mix for the second pellet (blue) raises the electron density at radii closer to the plasma center. In contrast, for double H_2 pellet injection (red), the density rise Δn_e in (e) is peaked more sharply and localized outside the zone where ablation light is observed in panel (d), which implies that the ablated material must have drifted outward afterward.

The pellets are injected radially from the LMFS, and the ablated material expands toroidally along the magnetic field lines. The spatially and temporally resolved FTS measurement can identify the radial profile of the electron density on the LMFS at the time when ablated material first arrives at the downstream toroidal position observed by the FTS. Here, this occurs about 0.3–0.4 ms after the first ablation light appears. The results are shown in Fig. 4. If there was no radially outward transport, the dense material would appear at the same radial position where it had been ablated from the pellet. However, in Fig. 4(a), we observe

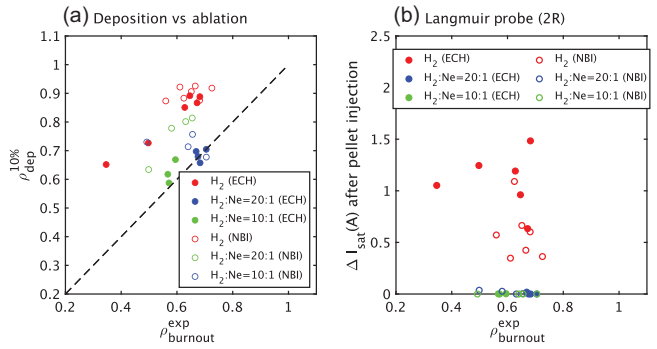

FIG. 5. (a) Radial depths $\rho_{\mathrm{dep}}^{10\%}$ (defined in the text) of the observed electron density rise versus the measured pellet burnout position $\rho_{\mathrm{burnout}}^{\mathrm{exp}}$. (b) Increment of the ion saturation current ΔI_{sat} after the pellet injection.

the n_e density peak from the first pure H_2 pellet around $R = 4.6$ m. At that radius, the electron temperature is too low to cause significant ablation of the pellet. Indeed, most of the ablation light (measured at the different toroidal angle) is seen in the region 4.1 m $\lesssim R \lesssim$ 4.6 m (the gray-shaded area). Therefore, the ablated material must have undergone radially outward transport before it reached the plasma cross section monitored by FTS. The density peak due to the second H_2 pellet in Fig. 4(a) exhibits slightly deeper deposition, but it is still far from the pellet's original penetration depth. In contrast, the blue curve in Fig. 4(b) indicates that the second $H_2 + Ne$ pellet clearly causes n_e to rise at the depth of the ablation light-emitted zone (indicated by the blue-shaded area). This shows that the $H_2 + Ne$ pellet directly fueled the ablation domain without being subject to any significant radially outward transport. This interpretation is also supported by the full sequence of FTS snapshots that covers the entire assimilation event and is provided in the Supplemental Material [46].

Data analysis and modeling.—Datasets for single $H_2 + Ne$ pellet injection consist of seven ECH and eight neutral beam injection (NBI) shots. They are compared here with datasets for pure H_2 injection, which consist of six ECH and seven NBI shots. The central T_{e0} varied between 1.1 and 8.0 keV. In Fig. 5(a), the radial depth ($\rho_{\mathrm{dep}}^{10\%}$) of the core density assimilation Δn_e is plotted versus the pellet burnout position ($\rho_{\mathrm{burnout}}^{\mathrm{exp}}$) obtained from the mapping of the ablation light to the normalized minor radius ρ, where we assume that the pellet travels in a plasma at the constant velocity measured by the light gate signals. Here, $\rho_{\mathrm{dep}}^{10\%}$ is defined by the normalized radius at which the normalized n_e increment value $f(\rho) = (\int_0^{\rho} \Delta n_e(\rho')(dV/d\rho)d\rho')/N_e$ obtained from the pre- and postinjection main TS data becomes 0.1 to characterize the inner envelope of the $\Delta n_e(\rho)$ profile (dV, the volume element; N_e, the total number of injected electrons). In Fig. 5(a), the mixed $H_2 + Ne$ pellets (blue, green) are seen to raise the electron density from the radial position close to the burnout position, $\rho_{\mathrm{dep}}^{10\%}(H_2 + Ne) \sim \rho_{\mathrm{burnout}}^{\mathrm{exp}}$, while pure H_2 pellets (red) yield

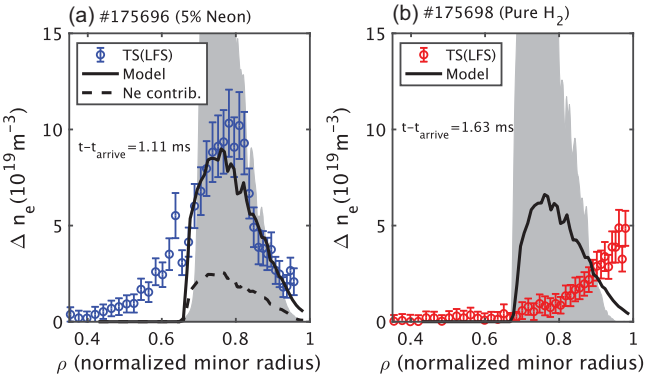

FIG. 6. Comparison of the Δn_e profiles from the main TS measurements and model calculations. The electron density from the ablation calculation [36] is computed assuming that the ablated material is deposited uniformly over the magnetic surfaces at the ablation position, and the contribution of neon to Δn_e (dashed curve) is obtained from a collisional-radiative equilibrium. For comparison, the ablation light emission (the gray-shaded profiles) observed at the upstream toroidal position is mapped to the normalized minor radius ρ.

only a density rise at $\rho_{\mathrm{dep}}^{10\%}(H_2) \sim 0.9$, except for a few outliers with deeper pellet penetration into ECH plasmas with relatively low T_e. This observation shows that the plasmoid drift, which leads to a mass relocation toward the outer minor radius for the H_2 pellets [18–24], is effectively absent for the $H_2 + Ne$ pellets. In our setup, the doped neon quantity is sufficiently small to have no effect on the pellet penetration depths. This facilitates a direct comparison of the two cases, which suggests that the mixed pellets can deposit their material deeper into the plasma.

Further evidence for the reduced outward material transport can be gleaned from the particle flux to the divertor plate, which is measured by increments of the Langmuir probe signals ΔI_{sat} following the ablation light after the pellet injection (see Fig. 3 of Ref. [42], for example). The results are plotted in Fig. 5(b). Enhanced particle fluxes are observed only after the injection of pure H_2 pellets (red). This is consistent with the fact that the $H_2 + Ne$ pellets (blue, green) are assimilated effectively in the core region, without significant particle losses to the divertor.

The absence of the outward radial transport simplifies modeling of the core density rise. Figure 6(a) shows that the postinjection electron density profile is reproduced reasonably well by the mere calculation of the ablation profiles using the numerical simulation code described in Ref. [36]. In contrast, Fig. 6(b) shows that the Δn_e profile after pure H_2 pellet injection cannot be reproduced by the ablation model alone, but would require extensions that account for the plasmoid drift and the relaxation of the internal energies and the electric field in dense plasmoids [23,24,39]. Finally, we note that the added neon can slow a pellet down and slightly reduces the ablation rate. However, both experimental data and ablation calculations in Fig. 6 show that differences in the ablation rates and pellet velocities encountered here are not significant enough to explain the observed difference depending on the pellet composition.

Discussion.—This study has experimentally demonstrated that a small fraction of neon added to hydrogenic pellets leads to the reduction of outward plasmoid transport. This result is consistent with the model calculation based on Ref. [36]: it has shown that the volume-averaged pressure of the plasmoid produced at the position where the ablation rate peaks in Fig. 6 ($\rho \simeq 0.7$) when it elongates over a half toroidal turn ($\simeq$15 m) is 45 kPa and 6.4 kPa for the pure H_2 and $H_2 + Ne$ pellets, respectively. In the latter case, the increased line radiation due to the added neon reduces the plasmoid pressure to a value comparable to the ambient plasma pressure ($\simeq$5–6 kPa), which suppresses the $\vec{E} \times \vec{B}$ transport of the ablated material that impacted earlier experiments on DIII-D using pure D_2 SPI. It should be emphasized that, because the local driving force for $\vec{E} \times \vec{B}$ drift is suppressed directly, the above mechanism is independent of the magnetic configuration and is applicable to tokamaks and stellarators alike.

Here, the use of a heliotron device, whose confining magnetic field is created without internal plasma currents, constitutes a key advantage, because the discharge is terminated nondisruptively even after impurity injection [47] and the plasmoid transport can be measured accurately. In a previous study on the DIII-D tokamak [48], the ablation of a pure neon pellet with a diameter of 1.8 mm was observed, showing that such a small fragment triggers a large-scale instability leading to a rapid thermal quench. Although the resultant density mixing is important to cause effective energy dissipation in the plasma center, such a global magnetohydrodynamic event obscures the local emission due to material ablation and complicates the diagnosis of the plasmoid transport.

ITER will employ the SPI scheme to deliver cryogenic materials, which shatters large pellets of a few cm into mm-sized fragments (comparable to single pellets studied here) for efficient ablation [49] just before the material enters the plasma. The observations made in our well-controlled experiments of cryogenic pellet ablation also offer a demonstration for how SPI supplies material into the core region when multiple fragments are injected as a bunch or cloud. The sequential injection reported in this Letter has experimentally demonstrated that the fragment injected just after the vanguard one can penetrate further and be assimilated at a deeper radial position.

In conclusion, the injection of mixed $H_2 + Ne$ pellets facilitates density assimilation at radii much deeper in the plasma than what was achieved with pure H_2 pellets alone. This effect is further boosted by multiple fragment injection like SPI, as trailing pellets were seen to penetrate farther than vanguard ones. In the present Letter, we used pellets with neon fractions of 5% and 10%. Although the optimal concentration for ITER and other experiments remains to

be determined, the present Letter has provided clear experimental evidence that this factor must be taken into consideration by optimization of the material injection for effective disruption mitigation in ITER. It is interesting to investigate how far the neon fraction can be reduced before one obtains results equivalent to those of pure H_2 pellets. The threshold is expected to depend on the target plasma temperature. The insight reported in this Letter may also be applied to study impurity seeding into a plasma by mixture pellets [5,50] for divertor power handling [51] and improved confinement [52] in future fusion reactors. In future studies, the FTS technique, which is based on advanced laser technology and was successfully applied in this Letter, is expected to serve as a powerful imaging tool.

One of the authors (A. M.) would like to thank A. Bierwage and M. Lehnen for their careful reading of the manuscript and J. Koga for useful suggestions. The experiments described in this Letter were supported by NIFS19/20/21ULPP004. This work was partially carried out under the auspices of the ITER Scientist Fellow Network and was supported in part by Grants-in-Aid for Scientific Research (MEXT KAKENHI Grant No. 21H01070).

*Corresponding author.
matsuyama.akinobu@qst.go.jp

[1] S. L. Milora, W. A. Houlberg, L. L. Lengyel, and V. Mertens, Nucl. Fusion **35**, 657 (1995).
[2] S. Sudo, N. Tamura, C. Suzuki, S. Muto, H. Funaba, and the LHD Experiment Group, Nucl. Fusion **52**, 063012 (2012).
[3] S. K. Combs and L. R. Baylor, Fusion Sci. Technol. **73**, 493 (2018).
[4] E. M. Hollmann, P. B. Parks, D. Shiraki, N. Alexander, N. W. Eidietis, C. J. Lasnier, and R. A. Moyer, Phys. Rev. Lett. **122**, 065001 (2019).
[5] P. T. Lang, B. Ploeckl, M. Bernert, A. Bock, R. Dux, A. Kallenbach, V. Rohde, M. Siccinio, W. Suttrop, and A. Zito (ASDEX Upgrade Team), Fusion Sci. Technol. **77**, 42 (2021).
[6] T. Luce, U. Kruezi, M. Lehnen, S. Jachmich, M. F. M. de Bock, and G. Ellwood, *Proceedings of the 28th IAEA Fusion Energy Conference* (Virtual Event, 2021) [Report No. TECH/1-4Ra].
[7] B. V. Kuteev, V. Yu. Sergeev, and S. Sudo, Nucl. Fusion **35**, 1167 (1995).
[8] R. Yoshino, T. Kondo, Y. Neyatani, K. Itami, Y. Kawano, and N. Isei, Plasma Phys. Controlled Fusion **39**, 313 (1997).
[9] M. Lehnen, K. Aleynikova, P. B. Aleynikov, D. J. Campbell, P. Drewelow, N. W. Eidietis, Yu. Gasparyan, R. S. Granetz, Y. Gribov *et al.*, J. Nucl. Mater. **463**, 39 (2015).
[10] ITER Organization, ITER research plan within the staged approach (Level III—Provisional Version), Report No. ITER-18-003, 2018, https://www.iter.org/technical-reports.
[11] E. Nardon, D. Hu, M. Hoelzl, D. Bonfiglio, and the JOREK team, Nucl. Fusion **60**, 126040 (2020).
[12] B. N. Breizman, P. Aleynikov, E. M. Hollmann, and M. Lehnen, Nucl. Fusion **59**, 083001 (2019).
[13] D. Shiraki, N. Commaux, L. R. Baylor, N. W. Eidietis, E. M. Hollmann, C. J. Lasnier, and R. A. Moyer, Phys. Plasmas **23**, 062516 (2016).
[14] J. Kim, L. R. Baylor, M. Lehnen, N. W. Eidietis, D. Shiraki, S. H. Park, J. W. Kim, J. W. Yoo, J. G. Bak *et al.*, *Proceedings of the 28th IAEA Fusion Energy Conference* (Virtual Event, 2021) [Report No. EX/5-3Ra].
[15] S. Jachmich, U. Kruezi, M. Lehnen, M. Baruzzo, L. R. Baylor, D. Carnevale, D. Craven, N. W. Eidietis, O. Ficker *et al.*, Nucl. Fusion **62**, 026012 (2022).
[16] H. W. Müller, K. Bühcl, M. Kaufmann, P. T. Lang, R. S. Lang, A. Lorenz, M. Maraschek, V. Mertens, J. Neuhauser (ASDEX Upgrade Team), Phys. Rev. Lett. **83**, 2199 (1999).
[17] V. Rozhansky, I. Veselova, and S. Voskoboynikov, Plasma Phys. Control. Fusion **37**, 399 (1995).
[18] L. R. Baylor, G. L. Schmidt, W. A. Houlberg, S. L. Milora, C. W. Gowers, W. P. Bailey, M. Gadeberg, P. Kupschus, J. A. Tagle *et al.*, Nucl. Fusion **32**, 2177 (1992).
[19] P. T. Lang, K. Büchl, M. Kaufmann, R. S. Lang, V. Mertens, H. W. Müller, J. Neuhauser (ASDEX Upgrade, and NI Teams), Phys. Rev. Lett. **79**, 1487 (1997).
[20] L. R. Baylor, T. C. Jernigan, S. K. Combs, W. A. Houlberg, M. Murakami, P. Gohil, K. H. Burrell, C. M. Greenfield, R. J. Groebner *et al.*, Phys. Plasmas **7**, 1878 (2000).
[21] P. B. Parks, W. D. Sessions, and L. R. Baylor, Phys. Plasmas **7**, 1968 (2000).
[22] A. R. Polevoi and M. Shimada, Plasma Phys. Controlled Fusion **43**, 1525 (2001).
[23] B. Pégourié, Plasma Phys. Controlled Fusion **49**, R87 (2007).
[24] P. B. Parks and L. R. Baylor, Phys. Rev. Lett. **94**, 125002 (2005).
[25] D. Shiraki, E. Hollmann, J. Herfindal, L. Baylor, N. Eidietis, Z. Popovic, C. Marini, A. Lvovskiy, J. Boedo *et al.*, *63rd Annual Meeting of the APS Division of Plasma Physics, Pittsburgh, 2021*.
[26] M. Scholer, Planet. Spac. Phys. **18**, 977 (1970).
[27] W. Peter and N. Rostoker, Phys. Fluids **25**, 730 (1982).
[28] M. Wickham and S. Robertson, Plasma Phys. **25**, 103 (1983).
[29] M. Galvez, Phys. Fluids **30**, 2729 (1987).
[30] J. E. Borovsky, Phys. Fluids **30**, 2518 (1987).
[31] J. F. Drake, M. Mulbrandon, and J. D. Huba, Phys. Fluids **31**, 3412 (1988).
[32] J. Koga, J. L. Geary, T. Fujinami, B. S. Newberger, T. Tajima, and N. Rostoker, J. Plasma Phys. **42**, 91 (1989).
[33] S. Y. Kim, Astrophys. Space Sci. **180**, 59 (1991).
[34] T. Neubert, R. H. Miller, O. Buneman, and K.-I. Nishikawa, J. Geophys. Res. **97**, 12057 (1992).
[35] R. Nishio and K. Suzuki, Phys. Fluids B **5**, 2036 (1993).
[36] A. Matsuyama, Phys. Plasmas **29**, 042501 (2022).
[37] A. Komori, H. Yamada, S. Imagawa, O. Kaneko, K. Kawahata, K. Mutoh, N. Ohyabu, Y. Takeiri, K. Ida *et al.*, Fusion Sci. Technol. **58**, 1 (2010).
[38] H. Yamada, A. Komori, N. Ohyabu, O. Kaneko, K. Kawahata, K. Y. Watanabe, S. Sakakibara, S. Murakami, K. Ida *et al.*, Plasma Phys. Controlled Fusion **43**, A55 (2001).

[39] A. Matsuyama, F. Koechl, B. Pégourié, R. Sakamoto, G. Motojima, and H. Yamada, Nucl. Fusion **52**, 123017 (2012).
[40] R. Sakamoto, G. Motojima, H. Hayashi, T. Inoue, Y. Ito, H. Ogawa, S. Takami, M. Yokota, and H. Yamada, Rev. Sci. Instrum. **84**, 083504 (2013).
[41] S. L. Milora and C. A. Foster, Rev. Sci. Instrum. **50**, 482 (1979).
[42] R. Sakamoto, H. Yamada, Y. Takeiri, K. Narihara, T. Tokuzawa, H. Suzuki, S. Masuzaki, S. Sakakibara, S. Morita *et al.*, Nucl. Fusion **46**, 884 (2006).
[43] I. Yamada, K. Narihara, H. Funaba, T. Minami, H. Hayashi, and T. Kohmoto (LHD Experiment Group), Fusion Sci. Technol. **58**, 345 (2010).
[44] R. Yasuhara, D. J. Den Hartog, H. Funaba, M. T. Borchardt, H. Uehara, D. J. Holly, T. D. Kile, T. Morisaki, and M. Osakabe, *Laser Aided Plasma Diagnostics (LAPD2019)* (Whitefish, 2019).
[45] H. Funaba, R. Yasuhara, H. Uehara, I. Yamada, R. Sakamoto, M. Osakabe, and D. J. Den Hartog, Sci. Rep. **12**, 15112 (2022).
[46] See Supplemental Material at http://link.aps.org/supplemental/10.1103/PhysRevLett.129.255001 for the full sequence of Fast Thomson Scattering (FTS) snapshots that measured the electron density profile evolution throughout the entire assimilation event for pure hydrogen and neon-doped hydrogen pellet injection.
[47] A. Dinklage, K. J. McCarthy, C. Suzuki, N. Tamura, Th. Wegner, H. Yamada, J. Baldzuhn, K. J. Brunner, B. Buttenschön *et al.*, Nucl. Fusion **59**, 076010 (2019).
[48] D. G. Whyte, T. E. Evans, A. W. Hyatt, T. C. Jernigan, R. L. Lee, A. G. Kellman, P. B. Parks, R. Stockdale, and P. L. Taylor, Phys. Rev. Lett. **81**, 4392 (1998).
[49] T. E. Gebhart, L. R. Baylor, and S. J. Meitner, IEEE Trans. Plasma Sci. **48**, 1598 (2020).
[50] A. Kallenbach, P. T. Lang, M. Bernert, R. Dux, T. Eberl, T. Gleiter, R. M. McDermott, C. Piccinni, B. Ploeckl *et al.*, Nucl. Fusion **62**, 106013 (2022).
[51] R. Wenninger, R. Albanese, R. Ambrosino, F. Arbeiter, J. Aubert, C. Bachmann, L. Barbato, T. Barrett, M. Beckeers *et al.*, Nucl. Fusion **57**, 046002 (2017).
[52] G. R. McKee, M. Murakami, J. A. Boedo, N. H. Brooks, K. H. Burrel, D. R. Ernst, R. J. Fonck, G. L. Jackson, M. Jakubowski *et al.*, Phys. Plasmas **7**, 1870 (2000).